ACS NANO
Cite This: ACS Nano 2019, 13, 8303–8311
www.acsnano.org

ARTICLE

Engineering Zero-Dimensional Quantum Confinement in Transition-Metal Dichalcogenide Heterostructures

Christopher C. Price,[†,#] Nathan C. Frey,[†,#] Deep Jariwala,[†,‡] and Vivek B. Shenoy*[,†]

[†]Department of Materials Science and Engineering, University of Pennsylvania, Philadelphia, Pennsylvania 19104, United States
[‡]Department of Electrical and Systems Engineering, University of Pennsylvania, Philadelphia, Pennsylvania 19104, United States

Supporting Information

Achieving robust, localized quantum states in two-dimensional (2D) materials like graphene is desirable for optoelectronics and quantum information yet challenging due to the difficulties in confining Dirac fermions. Traditional colloidal nanoparticle and epitaxially grown quantum dots are also impractical for solid-state devices, due to either complex surface chemistry, unreliable spatial positioning, or lack of electrical and optical access. In this work, we design and optimize nanoscale monolayer transition-metal dichalcogenide (TMD) heterostructures to natively host massive Dirac fermion bound states. We develop an integrated multiscale approach to translate first-principles electronic structure to higher length scales, where we apply a continuum model to consider arbitrary 2D quantum dot geometries and sizes. Focusing on a model system of an MoS_2 quantum dot in a WS_2 matrix (MoS_2/WS_2), we find discrete bound states in triangular dots with side lengths up to 20 nm. We propose figures of merit that, when optimized for, result in heterostructure configurations engineered for maximally isolated bound states at room temperature. These design principles apply to the entire family of semiconducting TMD materials, and we predict 6.5 nm MoS_2/WS_2 (quantum dot/matrix) triangular dots and 4.5 nm $MoSe_2/WSe_2$ triangular dots as ideal systems for confining massive Dirac fermions.

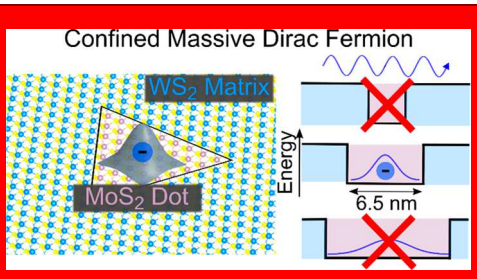

two-dimensional materials, quantum dot, transition-metal dichalcogenides, multiscale modeling, heterostructure, Dirac fermions

Initialization and manipulation of individual quantum states is a critical requirement to achieving high-performance optoelectronic devices and quantum information platforms. Thus far, engineering these states has primarily relied on generating deep level color centers/defects as quantum cavities in bulk materials[1] or physically reducing the semiconductor in all three dimensions to make nanocrystals.[2] The energetic tunability of these three-dimensional cavity states is well documented,[3] yet precise electrical or optical control of single quantum states remains elusive.[4,5] Two-dimensional (2D) materials are an attractive platform for quantum confinement due to their electronically stable surfaces and atomic-scale thickness, which provides perfect confinement in the out-of-plane dimension.[6] Graphene, the most extensively studied 2D material, hosts massless Dirac fermions, which cannot be localized because of carrier transmission regardless of the height or width of the potential barrier (Klein tunneling).[7−10] Several theoretical works have studied forced quantum confinement arising in idealized, isolated graphene disks and triangles with infinite mass gradients at the edges, which have not been experimentally realized.[11−13] Inducing quasi-confinement of relativistic Dirac fermions in graphene can be achieved by introducing a spatially varying bandgap *via* substrate effects (doping or spin−orbit coupling), strong magnetic or electric fields, or adding a second graphene layer.[9,14−17] However, this type of confinement is not a robust intrinsic property of the graphene system, the induced gaps are small (∼0.1 eV), and the extreme conditions required to accomplish quasi-confinement are impractical for technological applications.[18]

However, continued expansion of the 2D materials library has led to materials with properties distinct from graphene. The family of transition-metal dichalcogenide (TMD) monolayers contains many direct bandgap semiconductors with variable composition and tunable bandgaps which have been characterized using density functional theory (DFT) and tight-binding models.[19−23] In stark contrast to graphene, these systems host charge carriers that behave as massive Dirac fermions because the bandgap gives rise to an effective carrier mass that reduces the probability of Klein tunneling. Because these systems are isostructural with small variations in lattice

Received: May 13, 2019
Accepted: June 21, 2019
Published: June 21, 2019

DOI: 10.1021/acsnano.9b03716
ACS Nano 2019, 13, 8303–8311

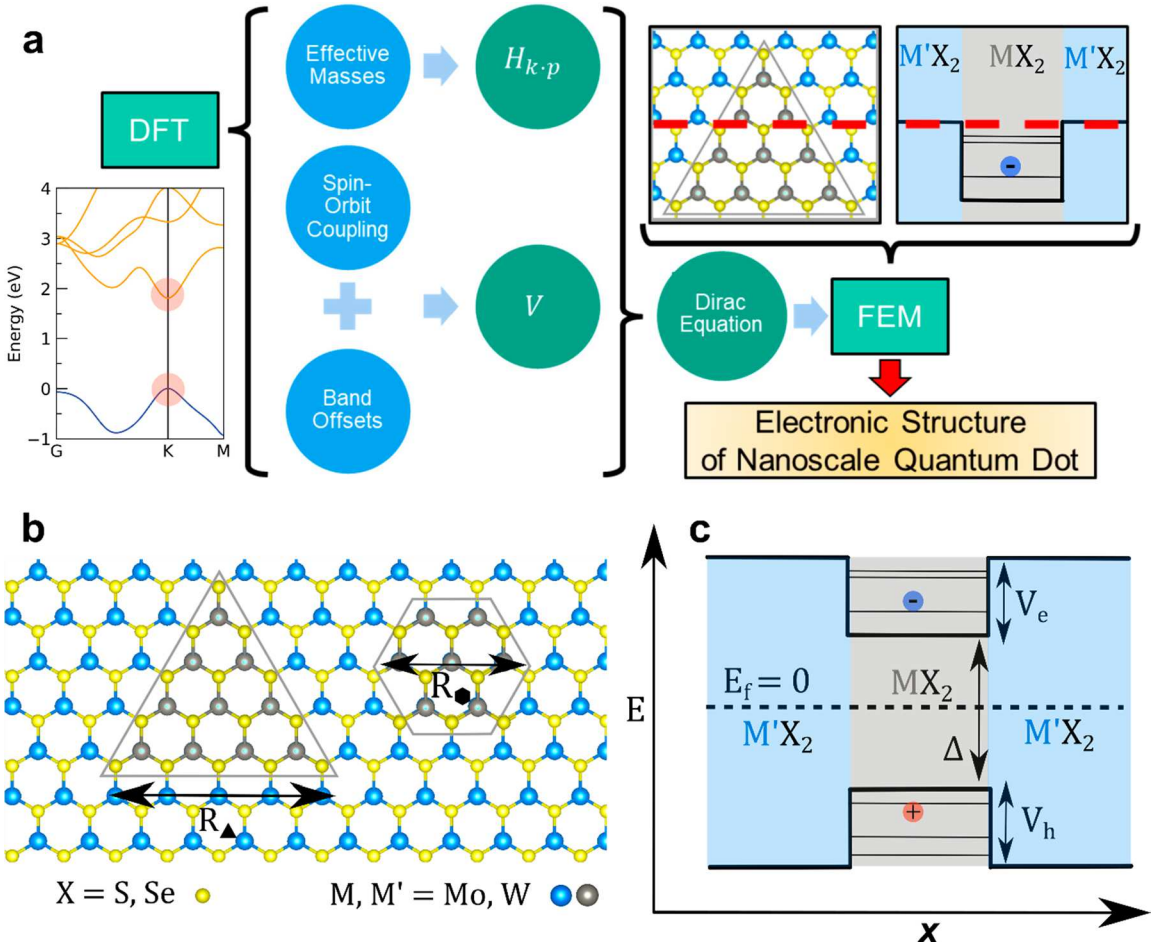

Figure 1. Schematic of the continuum approach to describing planar quantum dot electronic structure. (a) Parameters from DFT are used as inputs to a *k·p* model that is solved for device geometries with the finite element method. (b) Triangular and hexagonal regions of MX_2 in an $M'X_2$ matrix form 2D quantum dots. (c) The band offsets between MX_2 and $M'X_2$ create quantum wells for confining electrons and holes.

constant, we can envision structurally coherent in-plane quantum confinement engineered *via* van der Waals (vdW) heterostructuring[24] or lateral epitaxy.[25−27] The band offsets between different TMDs in a heterostructure can be exploited to construct a confining potential step due to the sharp change in the absolute band energies at a clean interface between the two materials. These Dirac carriers are physically distinct from the Schrödinger fermions encountered in epitaxial bulk semiconductor quantum dots[28] due to the symmetric degeneracies of the honeycomb lattice and the occurrence of the direct band gap at nonzero momentum (*K*-point).[29]

In this work, we develop a multiscale workflow to study the existence and evolution of the bound-state spectra of planar quantum dots engineered from TMD heterostructures as a function of their shape and size. The band structures are characterized by first-principles calculations, while tight binding and continuum models are used to describe realistic nanoscale device geometries that are inaccessible to DFT calculations. We explicitly show the bound-state energy scaling behavior for massive Dirac fermions in *finite potential wells* corresponding to an experimentally realizable vdW heterostructure. We find that the critical well size and well depth needed to support robust, isolated bound states are achievable in an MoS_2/WS_2 (quantum dot/matrix) heterostructure. Based on these results, we provide simple design rules for atomically thin TMD heterostructure quantum dots to achieve ideal quantum confinement.

RESULTS

Quantum Confinement in Monolayer TMDs and Lateral Heterostructures. First, we briefly discuss our approach to modeling quantum confinement in the TMD heterostructure. The computational workflow used here is represented schematically in Figure 1a. For any two TMDs, MX_2, and $M'X_2$, with direct band gaps at the high-symmetry *K* point, the band structures are calculated *via* DFT. The chalcogen X atom is chosen to be the same in both TMDs to minimize lattice mismatch and ensure that the band gaps remain direct.[30,31] The valence and conduction bands are fit around the *K* point to obtain the parameters (Table S1) for a two-band $\boldsymbol{k\cdot p}$ model, which captures the relevant physics of the conduction and valence bands in the *K* valley.[32] The details of the $\boldsymbol{k\cdot p}$ Hamiltonian up to second order in $\boldsymbol{k}$, $H^1_{kp}(\boldsymbol{k}) + H^2_{kp}(\boldsymbol{k})$, are given in the Methods section.

Figure 1b shows an atomistic model of the physical realization of a laterally confined TMD quantum dot system. A TMD with the formula unit MX_2 forms a nanoscale regular triangle or hexagon[33] within an $M'X_2$ matrix. The spatial extent of a quantum dot is defined by $R_▲$ and $R_⬢$, which gives the corner-to-corner distance of the minority material region. The band offsets between the two TMDs create the quantum

DOI: 10.1021/acsnano.9b03716
ACS Nano 2019, 13, 8303−8311

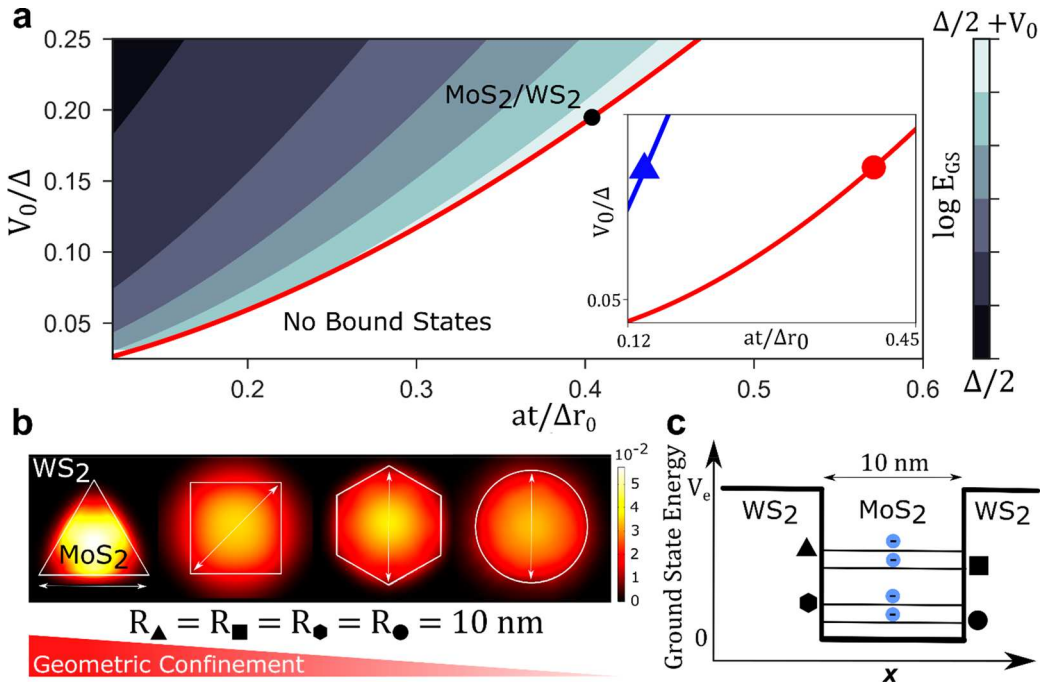

Figure 2. (a) Phase diagram for bound-state existence as a function of heterostructure parameters Δ (band gap), V_0 (confining potential magnitude), a (lattice constant), t (k·p hopping energy), and r_0 (dot radius) for the toy model circular finite well. The inset shows comparison with the bound-state existence boundary taken from numerical solutions for triangular wells. (b) Evolution of the ground state probability density showing decreasing localization with increased number of vertices for dots with equivalent corner-to-corner length. (c) Ground state energy relative to the continuum band edge corresponding to the dot geometries in (b).

confinement depicted in Figure 1c. To describe the spatially dependent band gap variation, we introduce an external finite potential term $V(\boldsymbol{x})$ given by

$$V(\boldsymbol{x}) = \begin{bmatrix} V_e(\boldsymbol{x}) & 0 \\ 0 & V_h(\boldsymbol{x}) \end{bmatrix} \tag{1}$$

where V_e is the conduction band offset and V_h is the valence band offset. $V(\boldsymbol{x})$ is zero inside the quantum dot and nonzero in the M′X_2 matrix. The magnitudes $|V_e|$ and $|V_h|$ control the strength of the confining potentials. If V_e is positive, there is a confining electron potential well in the quantum dot. Likewise, if V_h is negative, there is a confining hole potential well in the dot.

We consider two model systems for lateral quantum confinement: an MoS_2 dot in a WS_2 matrix (MoS_2/WS_2), and a WS_2 dot in an MoS_2 matrix (WS_2/MoS_2). The band offsets between these TMDs result in type 2 band alignment;[34] for MoS_2/WS_2, V_e = 0.31 eV, and for WS_2/MoS_2, V_h = −0.36 eV.[19] Thus, the first configuration yields an electron potential well, while the second forms a hole potential well. The model $H_{kp}(\boldsymbol{k}, \boldsymbol{x}) = H^1_{kp}(\boldsymbol{k}) + H^2_{kp}(\boldsymbol{k}) + V(\boldsymbol{x})$ can then be numerically solved in the COMSOL MULTIPHYSICS package for any device geometry or material combination, given the appropriate parameters.[11] The computed eigenvalues and eigenvectors correspond to the bound-state energies and wave functions of the quantum dot system.

Toy Model: 2D Massive Dirac Hamiltonian in a Radial Finite Potential Well. Our investigation into the existence of bound states in the MoS_2/WS_2 heterostructure begins with a simple toy model that emphasizes the unusual behavior of the massive Dirac fermions. It is well-known that for a particle in a finite potential well described by the Schrödinger equation, the ground state is bound for any arbitrarily shallow or narrow well in one or two dimensions.[35] On the contrary, due to particle−antiparticle conversion, bound-state existence is not guaranteed for Dirac fermions and depends explicitly on the form of the potential and the effective fermion mass. There is evidence that the existence of a bound ground state in 2D is uncertain even for simple radially symmetric potential wells.[36,37]

We construct a toy model of the MoS_2/WS_2 system by approximating the MoS_2 quantum dot as a circular region in a radially symmetric finite potential. Following DiVincenzo and Mele,[38] we solve the massive Dirac Hamiltonian for a finite potential to develop straightforward existence criteria for bound states in the MoS_2/WS_2 quantum disk system. For simplicity, we consider the simplified Hamiltonian $H(\boldsymbol{k}, \boldsymbol{r}) = H^1_{kp}(\boldsymbol{k}) + V(\boldsymbol{r})$ and set the finite band offset $V_e = V_h = V_0$, such that $V(r < r_0) = 0$ and $V(r > r_0) = V_0$, where r_0 is the radius of the MoS_2 dot and r is the radial coordinate. Since we are interested in potential well dimensions that support at least one bound state, we restrict the solution space to the ground state, where the angular quantum number $m = 0$. We apply continuity boundary conditions to the wave function at the well edge $r = r_0$ and look for bound-state solutions with energy E in the range $\frac{\Delta}{2} < E < \frac{\Delta}{2} + V_0$ To exclude quasi-bound states, we only allow terms in the wave function which exponentially decay as $r \to \infty$.[17] This leads to a transcendental equation for the bound state which must satisfy:

$$\frac{\mathrm{Re}[Y_0(-r_0\alpha_V)]}{J_0(r_0\alpha_W)} = \frac{i\alpha_V}{\alpha_W}\frac{E + \frac{\Delta}{2}}{V_0 - E - \frac{\Delta}{2}}\frac{\mathrm{Im}[Y_1(-r_0\alpha_V)]}{J_1(r_0\alpha_W)} \tag{2}$$

DOI: 10.1021/acsnano.9b03716
ACS Nano 2019, 13, 8303−8311

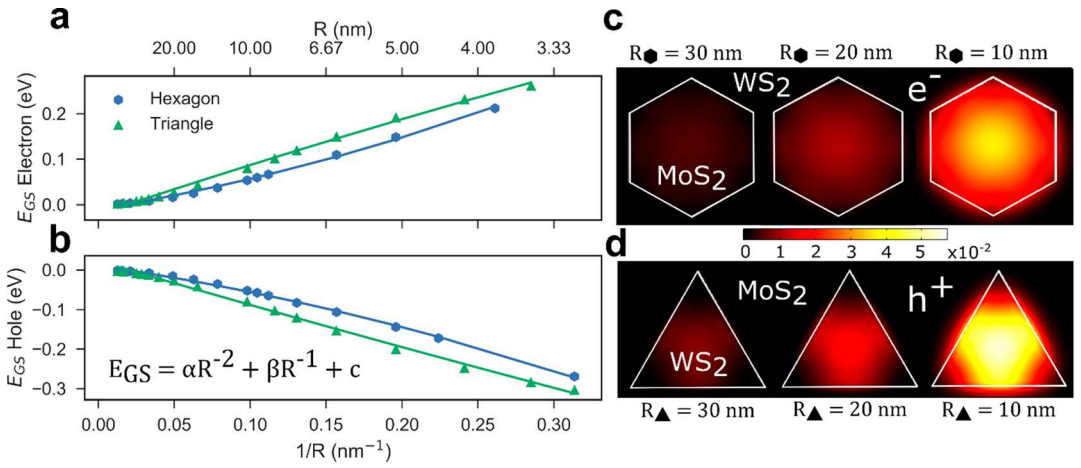

Figure 3. Scaling of the electron and hole ground states with inverse side length. (a) Electron and (b) hole ground state energies for triangular (green) and hexagonal (blue) quantum dots show a characteristic dependence on quantum dot size. (c) Electron and (d) hole ground state wave functions delocalize with increasing quantum dot size.

where $\alpha_W = \frac{\sqrt{E^2 - \left(\frac{\Delta}{2}\right)^2}}{at}$, $\alpha_V = \frac{\sqrt{E^2 - \left(\frac{\Delta}{2}\right)^2 - 2EV_0 + V_0^2}}{at}$. Here J_n and Y_n are the Bessel functions of the first and second kind, and Δ, a, and t are material parameters corresponding to the bandgap, lattice constant, and hopping energy taken from $H^1_{kp}(\boldsymbol{k})$. The limiting behavior and details of obtaining (eq 2) are discussed in the Supporting Information. We numerically solve for the roots of (eq 2) and plot (Figure 2a) the lowest bound-state energy as a function of the dimensionless quantities $\frac{V_0}{\Delta}$ and $\frac{at}{\Delta r_0}$. The phase map provides a completely general estimate of the ground state energy for any material parameters, with darker contours representing ground states closer to the bottom of the potential well and lighter contours approaching the top of the well.

In our model system of an MoS_2 dot in a WS_2 matrix, we find that minimum values of r_0 and V_0 define a phase boundary beyond which no bound states are supported. This behavior is particular to massive Dirac fermions in 2D. In contrast with a 2D Schrödinger quantum dot where confinement effectively disappears beyond some *maximum* diameter, in the Dirac quantum disk there is additionally a *minimum* critical size beyond which there is no confinement due to the Klein effect. This condition can also be achieved by taking Δ to 0 at finite V_0 and fixed size r_0, which recovers the massless graphene case. For the toy model MoS_2/WS_2 system with a conduction band offset $V_0 = V_e = 0.31$ eV, we find that the circular well has a critical radius of 2.6 Å, which is less than one unit cell. However, for more realistic quantum dot geometries that are not radially symmetric, the critical radius will be larger. In the limit of small r_0, breaking the radial symmetry of the quantum disk and introducing a three-fold rotational symmetry shifts the critical bound-state phase boundary in a nontrivial way, increasing the minimum critical size for the MoS_2/WS_2 system from 0.5 to 1.5 nm (Figure 2a, inset). These critical sizes are highly dependent on the band offset, and the criteria are more restrictive for confining wells with smaller band offsets. Having shown the existence of bound states for massive fermions in TMD heterostructures, we next turn to exploring the effects of realistic quantum dot geometries on confinement.

Bound-State Spectra in Triangular and Hexagonal Dots – Continuum Approach. Several different quantum dot geometries are accessible based on the crystal symmetry of the component TMD materials and synthesis conditions.[33] We compute the ground state using the continuum method for a circular quantum dot, finding quantitative agreement with the toy model results ($E_{\text{analytic}} - E_{\text{continuum}} = 0.5$ meV, which equals the $E(H^2_{kp})$ correction absent from the toy model), and then repeat the process for hexagonal, square, and triangular geometries. Figure 2b shows the evolution of the ground state wave function as the number of vertices in the dot geometry increases from three (triangle) to infinity (circle), with the vertex–vertex distance fixed at 10 nm (significantly above the bound-state existence boundary). At this size, at least one bound state is present for the MoS_2/WS_2 system in all geometries, but as shown in Figure 2c, the energy of this state relative to the band offset varies considerably. This is primarily explained by the fact that the dot area is minimized for a given vertex–vertex length in the triangle, and this reduction in area manifests as an effective geometric confinement. The sensitivity of the ground state energy to this geometrical effect is an important consideration for device design, as the transition from a hexagonal dot to a triangular dot (two common geometries in TMD flake systems)[39,40] in the model system increases the ground state energy by a factor of almost three (30 meV *vs* 80 meV). Therefore, the triangular system is better for engineering confinement at larger dot sizes, which may be advantageous for experimental observations.

Since triangular and hexagonal shapes are most commonly observed for TMD monolayers due to the hexagonal unit cell, we focus on these geometries to investigate the evolution of the electron and hole ground states with system size. To engineer quantum confinement, we determine the maximum and optimal dot sizes for hosting bound states. We systematically vary $R_\blacktriangle$ and $R_\hexagon$ and compute the ground state energies for each geometry. The electron (Figure 3a) and hole (Figure 3b) ground state energies are plotted *vs* inverse side length for triangular (green points) and hexagonal (blue points) geometries to show the characteristic scaling. The corresponding $R_\blacktriangle$ and $R_\hexagon$ values are given on the upper x-axis for convenience. Rescaling the energies such that $\frac{\Delta}{2}$ (the bottom of the well) corresponds to 0, we see a monotonic decrease in the electron ground state with increasing dot size. For small dots ($R_\blacktriangle < 5$ nm), the ground state energy is close to the top of the electron well. The quantum confinement

DOI: 10.1021/acsnano.9b03716
ACS Nano 2019, 13, 8303–8311

persists for large dots ($R_{\blacktriangle}$ > 20 nm), as the ground state approaches the bottom of the potential well. This confinement predicted for large nanoscale geometries is a consequence of the ideal confinement in the out-of-plane direction in these 2D structures, despite the finite nature of the potential barrier and relativistic properties of the carriers.

The ground state energy dependence on quantum dot size follows the simple relation:

$$E_{gs}(R) = \alpha R^{-2} + \beta R^{-1} + c \quad (3)$$

where R is length, α and β are materials-dependent constants, and c is a constant specified to set the bottom of the potential well equal to zero. This scaling with inverse length and inverse length squared follows immediately from the expansion in $\boldsymbol{k}$ (which has units of inverse length) in the $\boldsymbol{k}\cdot\boldsymbol{p}$ model. The ground state energy for any geometry is then totally specified by the α and β coefficients for a given $MX_2/M'X_2$ pair. The same characteristic scaling behavior is seen for holes in WS_2/MoS_2 (Figure 3b).

Visualizing the ground state wave functions provides a qualitative picture of the extent of quantum confinement. Figure 3c shows the electron ground state wave function in hexagonal MoS_2 quantum dots with $R_{\hexagon}$ = 10, 20, and 30 nm. At $R_{\hexagon}$ = 10 nm, the wave function is strongly localized. The amplitude is large at the center of the dot and radially decays, as expected. As the area of the hexagon increases, the wave function becomes increasingly delocalized until confinement is no longer apparent. At this point, the ground state of the system is indistinguishable from the infinite periodic band structure, and the finite dot region is no longer discretely quantized. The same wave function delocalization is observed for hole ground states in triangular WS_2 dots with increasing area (Figure 3d).

To verify the validity (and limitations) of the continuum approach, we repeat the analysis at small dot sizes using a three-band tight-bonding model[32] of a triangular MoS_2 quantum dot[41] with an outer edge of WS_2 atoms that forms the finite electron confining well. We recover the same characteristic ground state energy scaling described by (eq 3) in the tight binding model results (Figure S1b). The computed wave functions (Figure S1c) agree with those from the continuum model, although the inclusion of an additional d band and spin−orbit coupling in the tight-binding model leads to degeneracy breaking in the excited states. Importantly, while $\boldsymbol{k}\cdot\boldsymbol{p}$ is a long wavelength theory that is expected to break down at small length scales, the tight-binding approach describes the quantum dot system at these length scales. The continuum approach is well-suited for device-relevant length scales, so there seem to be no apparent gaps in our multiscale approach. Independently, we verify the validity of the truncation of the $\boldsymbol{k}$ expansion to second order by measuring the magnitude of the correction introduced by $H^2_{kp}(\boldsymbol{k})$ as a function of dot size (Figure S2). As expected, the higher order terms are more important for smaller dot sizes, and for a 4 nm MoS_2/WS_2 triangular dot, the second-order correction reaches a maximum of 8.5 meV, which is well within the perturbative regime. At small dot sizes in the tight-binding regime, the higher order terms in the continuum model will affect the quantitative energy values, but overall trends such as the geometry-critical size relationships are minimally impacted.

Having considered the ground state energy-size scaling for electrons and holes, we reduce the model MoS_2/WS_2 system to just triangular dots and consider the complete bound-state spectrum as a function of dot size. To compute all of the bound states, we iteratively solve the eigenvalue problem over the entire range of energies in the potential well and extract the smooth eigenstates. Figure 4a shows some representative

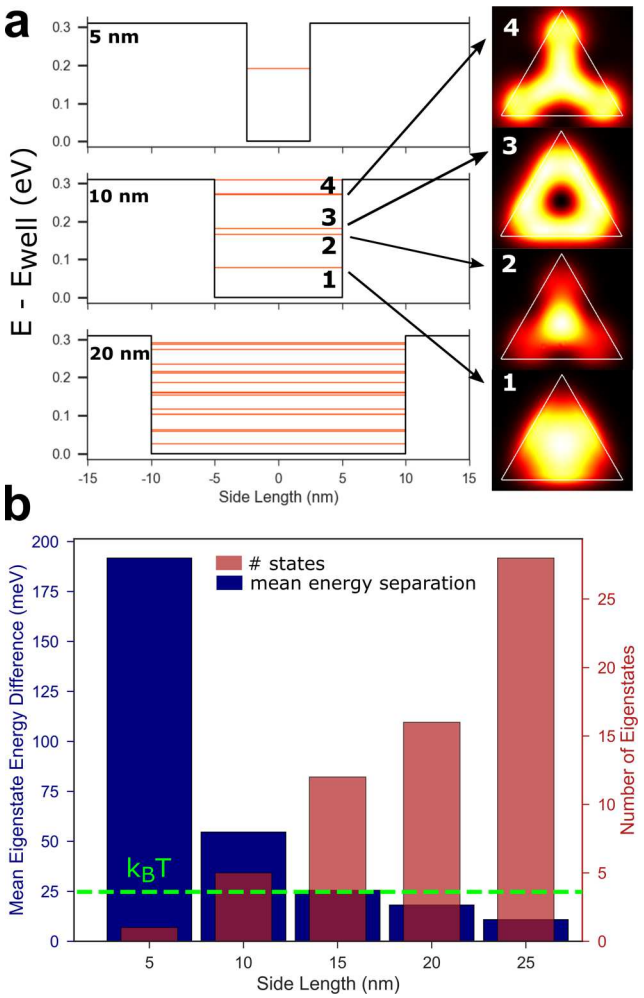

Figure 4. (a) Bound-state spectra for MoS_2/WS_2 triangular quantum dots as a function of dot size. A sample of wave functions is shown for the 10 nm well; wave functions possess three-fold rotational symmetry of the confining geometry. (b) Bound-state energy spacing and effective density of states *vs* size of the dots in (a). The average state spacing rapidly drops below k_BT @ 300 K as the confinement decreases.

bound-state spectra with energies referenced to the bottom of the well ($M'X_2$ band edge). At a 5 nm side length (Figure 4a, top), the MoS_2 well effectively supports only one bound state, with an additional bound state appearing at the very top of the potential well. As the MoS_2 well region is enlarged, the number of bound states increases, and the energy of the ground state reduces toward the energy of the pristine monolayer band edge. Figure 4a also shows the probability density of the electron wave functions, $|\Psi_e|^2$, corresponding to the first 4 eigenstates of the confined system. The closely spaced states visible near eigenstate 2 and 3 are due to differing contributions from the valence band wave function with different angular momentum quantum numbers; this occurs at all higher energy eigenstates, but the energy splitting is small. Due to the inclusion of $H^2_{kp}(\boldsymbol{k})$, we avoid the common fermion

DOI: 10.1021/acsnano.9b03716
ACS Nano 2019, 13, 8303−8311

doubling problem that arises in discretizing Dirac Hamiltonians by introducing an effective Wilson mass.[42] As expected, the symmetry of the excited eigenstates matches the confining geometry of the finite potential well. Examples for hole wave functions in hexagonal confined WS_2 dots are given in the Supporting Information. At 20 nm (Figure 3a, bottom), the eigenstates are collapsing into a continuum description. At this size, the high area to depth ratio of the well means that the potential step at the well edges is no longer impacting the wave function in the center of the well.

Figure 4c gives a quantitative description of the bound-state spectrum evolution with increasing dot size from 5 to 25 nm. The blue columns show the average energy spacing between eigenstates for a particular dot size, including the energy separation between the ground state and the well bottom. For a fixed well depth, the average energy spacing between states decreases rapidly with increasing side length, crossing $k_BT \cong$ 25 meV at 15 nm, which means that the average state is no longer thermally isolated at room temperature. The red columns give the number of bound states in the well as the side length increases up to 25 nm, when the ground state is within k_BT of the continuum band edge and effectively merges with the continuum. In the design and synthesis of solid-state quantum dots for optoelectronic applications, this threshold should be kept in mind as a heuristic to minimize thermally induced decoherence due to increasing density of states near the desired excitation. Akin to the determination of the critical maximum size for confinement, this threshold arising from neighboring excited bound states places a restrictive practical constraint on feasible quantum dot configurations.

Synthesizing the results presented above, we outline a general design scheme in Figure 5 to optimize quantum confinement in 2D semiconductor heterostructures. For any combination of layered TMD semiconductors, absolute band energies and $\boldsymbol{k}\cdot\boldsymbol{p}$ parameters can be obtained from first-principles calculations on pristine periodic systems (Figure 5a). From these parameters, finite size effects can be explored at length scales that are experimentally accessible but beyond the scope of DFT calculations or tight-binding models. From the phase diagram in Figure 2, bound-state existence can be determined based on the DFT parameters for the pristine monolayers. If bound states exist, then we can assess the robustness of the planar quantum dot confinement using two basic figures of merit: $F_1 = \left|\frac{\Delta E_{gs}}{V_{well}} - 0.5\right|$, the percent deviation of the ground state from the center of the well, and $F_2 = \Delta E_{es-gs}$, the energy spacing between the ground state and the first excited state (Figure 5b). These metrics characterize the degree of isolation for a quantum state that is energetically centered between the band edges of the component materials. An optimal, isolated state has the best chance of withstanding perturbations caused by edge states or atomic defects, without knowing *a priori* where the dominant defect levels exist for a given semiconductor heterostructure. To achieve such a state, we need to simultaneously minimize F_1 and maximize F_2. Figure 5c,d plots F_1 and F_2 as a function of the dimensionless scaling variables $at/\Delta r_0$ and V/Δ, where V is the band offset in the confining well, along with examples of TMD heterostructures based on their band structure parameters. Since the band offsets are not identical for TMD heterostructures as they were in our toy model (Figure 2), and there is some mixing between the two bands, this parametrization lacks a dependence on the difference between V_h and V_e. We take $V_0 \approx V_{e(h)}$ for confined electrons (holes) to preserve simplicity, because the $V_e - V_h$ coupling correction to the ground state energy is small.

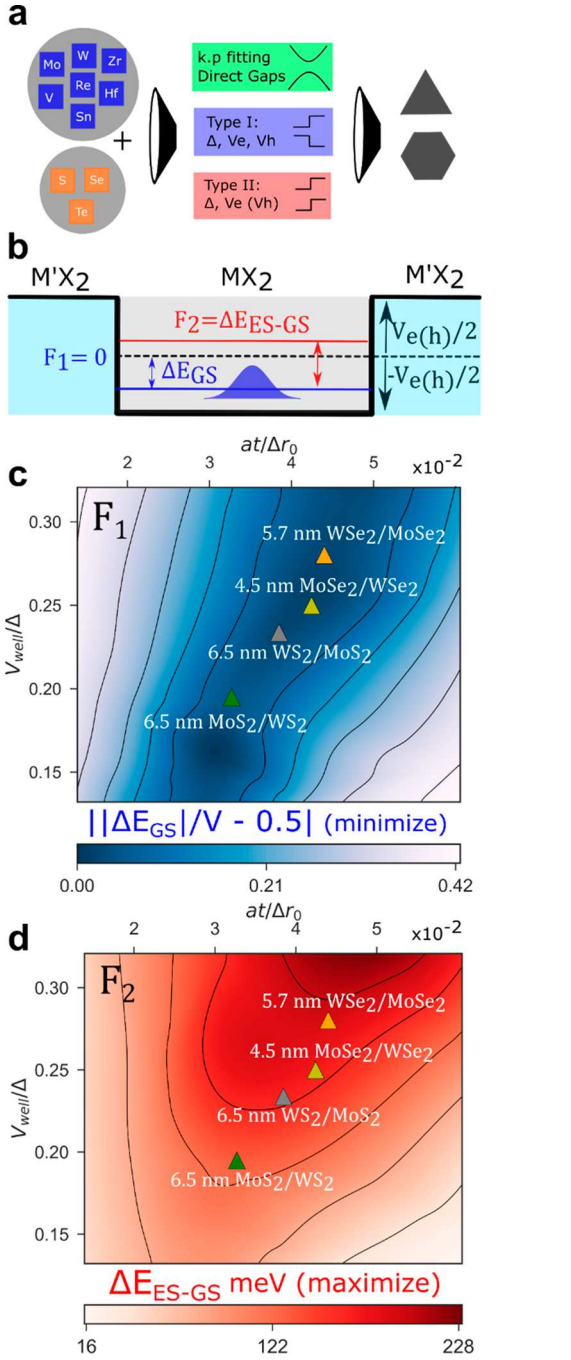

Figure 5. (a) Design workflow for forming confining TMD heterostructures. (b) Figures of merit for evaluating the performance of an MX_2 quantum dot in isolating a single quantum state. $\frac{\Delta E_{gs}}{V} - 0.5$ measures the percent deviation from the center of the well, and ΔE_{es-gs} gives the energy separation between the ground state and the first excited state. (c, d) Design optimization diagrams for the figures of merit in (b), with results for different TMD heterostructures in several dot configurations overlaid.

For type II band alignment, the optimization shows that deeper wells (corresponding to a larger band misalignment between the two semiconductors) lead to greater energy separation between the ground and first excited states at a fixed

DOI: 10.1021/acsnano.9b03716
ACS Nano 2019, 13, 8303−8311

dot area. The same is true for the ground state energy spacing from the well bottom. In the MoS_2/WS_2 system, there is an optimum triangular side length of ~6.5 nm that corresponds to the maximally centered ground state in the middle of the well, whereas for $MoSe_2/WSe_2$, this optimum size is closer to 4.5 nm. TMD monolayer flakes with spatial extent <10 nm have been synthesized, making these systems both practical and ideal for nanoscale quantum confinement.[43−48] Recently, both bottom-up[25,49] and top-down[50,51] approaches have demonstrated high control over 2D heterostructure features on this length scale, within the bounds of the kT threshold identified in Figure 4b.

The optimal size asymmetry between confined electrons and holes in the selenide system arises from a change in the hopping energy between the molybdenum and tungsten compounds. In the sulfide system, a similar hopping energy difference is counterbalanced by a change in the band gap which does not occur in the selenide system. In smaller dots at constant band offset, the ground state approaches the top of the well, eventually leading to the phase boundary for bound state existence seen in Figure 2. Furthermore, increasing the lattice constant or hopping energy at a fixed offset also increases the confinement for a fixed geometry. For shallow wells, larger dot sizes are preferable to realize bound states far from the background band edges, which may have relevance for Moiré superlattice engineering. Overall, these findings lead to the surprising and important conclusion that, rather than naively minimizing the dot area, optimal confinement is achieved by tuning the quantum dot spatial extent to a precise value that depends sensitively on the material parameters.

CONCLUSIONS

In this paper, we have presented and analyzed a lateral TMD heterostructure architecture for ideal quantum confinement. In doing so, we demonstrated a multiscale computational approach for optimizing realistic material and device parameters to achieve robust, coherent single quantum states in ambient conditions. By considering a toy model of a 2D quantum well, we established the criteria for supporting bound states in a TMD heterostructure and clearly emphasized the advantage of intrinsic confinement of massive Dirac fermions, compared to graphene which supports only quasi-bound states under applied fields. With a continuum method for solving a two-band $\boldsymbol{k}\cdot\boldsymbol{p}$ model, geometric effects were shown to play an important role in engineering robust confinement, with triangular 2D quantum dots exhibiting maximal geometric confinement. The ground state energies scale with the system size as $\alpha R^{-2} + \beta R^{-1}$, such that the lowest bound-state energy can be predicted for any size and shape of quantum dot simply by computing the material dependent coefficients α and β *via* fitting to continuum results. Performance metrics for confinement were proposed in terms of the energetic isolation of the ground state from both bulk band edges and neighboring excited states. Optimizing for these metrics in an MoS_2 triangular quantum dot in a WS_2 matrix results in a prediction of ~6.5 nm side length for optimal confinement. Moreover, we predict optimal geometries for arbitrary heterostructures of TMDs, and our formalism can easily be applied to any 2D semiconductor heterostructure. Our findings establish straightforward design principles for engineering optimal 2D quantum confinement at room temperature that should be of immediate use in the experimental realization of coherent quantum states.

METHODS

The two-band $\boldsymbol{k}\cdot\boldsymbol{p}$ model to first order in $\boldsymbol{k}$ corresponds to a massive Dirac Hamiltonian, H, which captures the salient structure of the K valley in MoS_2,[21] while the second-order contribution describes the anisotropic dispersion and electron−hole asymmetry, and including the third-order contribution completely recovers the DFT band structure.[23,32,52] We ignore the spin degree of freedom (reducing H to a 2×2 matrix) and spin−orbit coupling and include contributions up to second order in $\boldsymbol{k}$, such that the model is given by[32]

$$H^1_{kp}(\boldsymbol{k}) = \begin{bmatrix} \frac{\Delta}{2} & at(k_x - ik_y) \\ at(k_x + ik_y) & -\frac{\Delta}{2} \end{bmatrix} \tag{4}$$

$$H^2_{kp}(\boldsymbol{k}) = a^2 \begin{bmatrix} \gamma_1 k^2 & \gamma_3(k_x + ik_y)^2 \\ \gamma_3(k_x - ik_y)^2 & \gamma_2 k^2 \end{bmatrix} \tag{5}$$

where Δ is the direct band gap, a is the lattice constant, t is the hopping parameter, $\gamma_1 - \gamma_3$ are energy parameters, and $k^2 = k_x^2 + k_y^2$. With the Fermi level in the middle of the gap set to zero, the valence band maximum and conduction band minimum of MX_2 are $-\Delta/2$ and $\Delta/2$, respectively, where the band gap of the MX_2 quantum dot is Δ. The top (or bottom) of the potential well is then $\Delta/2 + V_e$ or $-\Delta/2 - V_h$ for electrons or holes, respectively.

The tight-binding model was constructed by considering nearest-neighbor hopping between Mo d_{z^2}, d_{xy}, and $d_{x^2-y^2}$ orbitals.[32] The tight-binding Hamiltonian for the finite triangular quantum dot includes diagonal submatrices that account for the on-site energies, spin−orbit coupling, and an external scalar potential $V(\boldsymbol{x})$ and off-diagonal submatrices that describe the directional hopping between Mo d orbitals.[41] The external potential was adjusted on the outermost edge of atoms to model the band offset between Mo and W.

ASSOCIATED CONTENT

Supporting Information

The Supporting Information is available free of charge on the ACS Publications website at DOI: 10.1021/acsnano.9b03716.

Ground state energy scaling calculated using a tight-binding approach; contributions of second-order correction to H *vs* system size; excited bound states for a hexagonal dot; tables of material parameters used and scaling coefficients calculated; detailed derivation of toy model used to plot Figure 2a (PDF)

AUTHOR INFORMATION

Corresponding Author

*E-mail: vshenoy@seas.upenn.edu.

ORCID

Christopher C. Price: 0000-0002-4702-5817

Nathan C. Frey: 0000-0001-5291-6131

Deep Jariwala: 0000-0002-3570-8768

Author Contributions

#These authors contributed equally to the work.

Funding

This work is supported primarily by contract W911NF-16-1-0447 from the Army Research Office (V.B.S.) and also by grants EFMA-542879 and CMMI-1727717 from the U.S. National Science Foundation. N.C.F. was supported by the Department of Defense (DoD) through the National Defense Science and Engineering Graduate Fellowship (NDSEG) Program. D.J. acknowledges primary support for this work by

DOI: 10.1021/acsnano.9b03716
ACS Nano 2019, 13, 8303−8311

the U.S. Army Research Office under contract number W911NF1910109.

Notes

The authors declare no competing financial interest.

REFERENCES

(1) Hennessy, K.; Badolato, A.; Winger, M.; Gerace, D.; Atatüre, M.; Gulde, S.; Fält, S.; Hu, E. L.; Imamoğlu, A. Quantum Nature of a Strongly Coupled Single Quantum Dot−Cavity System. *Nature* **2007**, *445*, 896−899.

(2) Alivisatos, A. P. Semiconductor Clusters, Nanocrystals, and Quantum Dots. *Science* **1996**, *271*, 933−937.

(3) Jasieniak, J.; Smith, L.; Van Embden, J.; Mulvaney, P.; Califano, M. Re-Examination of the Size-Dependent Absorption Properties of CdSe Quantum Dots. *J. Phys. Chem. C* **2009**, *113*, 19468−19474.

(4) Kurtsiefer, C.; Mayer, S.; Zarda, P.; Weinfurter, H. Stable Solid-State Source of Single Photons. *Phys. Rev. Lett.* **2000**, *85*, 290−293.

(5) Senellart, P.; Solomon, G.; White, A. High-Performance Semiconductor Quantum-Dot Single-Photon Sources. *Nat. Nanotechnol.* **2017**, *12*, 1026−1039.

(6) Gupta, A.; Sakthivel, T.; Seal, S. Recent Development in 2D Materials beyond Graphene. *Prog. Mater. Sci.* **2015**, *73*, 44−126.

(7) Novoselov, K. S.; Bostwick, A.; Seyller, T.; Horn, K.; Rotenberg, E. Electric Field Effect in Atomically Thin Carbon Films. *Science* **2004**, *306*, 666−669.

(8) Katsnelson, M. I.; Novoselov, K. S.; Geim, A. K. Chiral Tunnelling and the Klein Paradox in Graphene. *Nat. Phys.* **2006**, *2*, 620−625.

(9) Lee, J.; Wong, D.; Velasco, J., Jr; Rodriguez-Nieva, J. F.; Kahn, S.; Tsai, H.-Z.; Taniguchi, T.; Watanabe, K.; Zettl, A.; Wang, F.; Levitov, L. S.; Crommie, M. F. Imaging Electrostatically Confined Dirac Fermions in Graphene Quantum Dots. *Nat. Phys.* **2016**, *12*, 1032−1036.

(10) Gutiérrez, C.; Brown, L.; Kim, C.-J.; Park, J.; Pasupathy, A. N. Klein Tunnelling and Electron Trapping in Nanometre-Scale Graphene Quantum Dots. *Nat. Phys.* **2016**, *12*, 1069−1075.

(11) Zarenia, M.; Chaves, A.; Farias, G. A.; Peeters, F. M. Energy Levels of Triangular and Hexagonal Graphene Quantum Dots: A Comparative Study between the Tight-Binding and Dirac Equation Approach. *Phys. Rev. B: Condens. Matter Mater. Phys.* **2011**, *84*, 245403.

(12) Milton Pereira, J.; Vasilopoulos, P.; Peeters, F. M. Tunable Quantum Dots in Bilayer Graphene. *Nano Lett.* **2007**, *7*, 946−949.

(13) Pereira, J. M.; Mlinar, V.; Peeters, F. M.; Vasilopoulos, P. Confined States and Direction-Dependent Transmission in Graphene Quantum Wells. *Phys. Rev. B: Condens. Matter Mater. Phys.* **2006**, *74*, 045424.

(14) Kim, K. S.; Walter, A. L.; Moreschini, L.; Seyller, T.; Horn, K.; Rotenberg, E.; Bostwick, A. Coexisting Massive and Massless Dirac Fermions in Symmetry-Broken Bilayer Graphene. *Nat. Mater.* **2013**, *12*, 887−892.

(15) Zhou, S. Y.; Gweon, G.-H.; Fedorov, A. V.; First, P. N.; de Heer, W. A.; Lee, D.-H.; Guinea, F.; Castro Neto, A. H.; Lanzara, A. Substrate-Induced Bandgap Opening in Epitaxial Graphene. *Nat. Mater.* **2007**, *6*, 770−775.

(16) Recher, P.; Nilsson, J.; Burkard, G.; Trauzettel, B. Bound States and Magnetic Field Induced Valley Splitting in Gate-Tunable Graphene Quantum Dots. *Phys. Rev. B: Condens. Matter Mater. Phys.* **2009**, *79*, 085407.

(17) Matulis, A.; Peeters, F. M. Quasibound States of Quantum Dots in Single and Bilayer Graphene. *Phys. Rev. B: Condens. Matter Mater. Phys.* **2008**, *77*, 115423.

(18) Pedersen, T. G.; Jauho, A.-P.; Pedersen, K. Optical Response and Excitons in Gapped Graphene. *Phys. Rev. B: Condens. Matter Mater. Phys.* **2009**, *79*, 113406.

(19) Zhang, C.; Gong, C.; Nie, Y.; Min, K.-A.; Liang, C.; Oh, Y. J.; Zhang, H.; Wang, W.; Hong, S.; Colombo, L.; Wallace, R. M.; Cho, K. Systematic Study of Electronic Structure and Band Alignment of Monolayer Transition Metal Dichalcogenides in Van Der Waals Heterostructures. *2D Mater.* **2017**, *4*, 015026.

(20) Bieniek, M.; Korkusiński, M.; Szulakowska, L.; Potasz, P.; Ozfidan, I.; Hawrylak, P. Band Nesting, Massive Dirac Fermions, and Valley Landé and Zeeman Effects in Transition Metal Dichalcogenides: A Tight-Binding Model. *Phys. Rev. B: Condens. Matter Mater. Phys.* **2018**, *97*, 85153.

(21) Xiao, D.; Liu, G.-B.; Feng, W.; Xu, X.; Yao, W. Coupled Spin and Valley Physics in Monolayers of MoS_2 and Other Group-VI Dichalcogenides. *Phys. Rev. Lett.* **2012**, *108*, 196802.

(22) Liu, G.-B.; Shan, W.-Y.; Yao, Y.; Yao, W.; Xiao, D. Three-Band Tight-Binding Model for Monolayers of Group-VIB Transition Metal Dichalcogenides. *Phys. Rev. B: Condens. Matter Mater. Phys.* **2013**, *88*, 85433.

(23) Kormányos, A.; Zólyomi, V.; Drummond, N. D.; Rakyta, P.; Burkard, G.; Fal'ko, V. I. Monolayer MoS_2: Trigonal Warping, the Valley, and Spin-Orbit Coupling Effects. *Phys. Rev. B: Condens. Matter Mater. Phys.* **2013**, *88*, 45416.

(24) Jariwala, D.; Sangwan, V. K.; Lauhon, L. J.; Marks, T. J.; Hersam, M. C. Emerging Device Applications for Semiconducting Two-Dimensional Transition Metal Dichalcogenides. *ACS Nano* **2014**, *8*, 1102−1120.

(25) Xie, S.; Tu, L.; Han, Y.; Huang, L.; Kang, K.; Lao, K. U.; Poddar, P.; Park, C.; Muller, D. A.; DiStasio, R. A.; Park, J. Coherent, Atomically Thin Transition-Metal Dichalcogenide Superlattices with Engineered Strain. *Science* **2018**, *359*, 1131−1136.

(26) Zhang, Z.; Chen, P.; Duan, X.; Zang, K.; Luo, J.; Duan, X. Robust Epitaxial Growth of Two-Dimensional Heterostructures, Multiheterostructures, and Superlattices. *Science* **2017**, *357*, 788−792.

(27) Gong, Y.; Lin, J.; Wang, X.; Shi, G.; Lei, S.; Lin, Z.; Zou, X.; Ye, G.; Vajtai, R.; Yakobson, B. I.; Terrones, H.; Terrones, M.; Tay, B. K.; Lou, J.; Pantelides, S. T.; Liu, Z.; Zhou, W.; Ajayan, P. M. Vertical and In-Plane Heterostructures from WS_2/MoS_2 Monolayers. *Nat. Mater.* **2014**, *13*, 1135−1142.

(28) Wang, L.-W.; Zunger, A. High-Energy Excitonic Transitions in CdSe Quantum Dots. *J. Phys. Chem. B* **1998**, *102*, 6449−6454.

(29) Mei, J.; Wu, Y.; Chan, C. T.; Zhang, Z.-Q. First-Principles Study of Dirac and Dirac-like Cones in Phononic and Photonic Crystals. *Phys. Rev. B: Condens. Matter Mater. Phys.* **2012**, *86*, 035141.

(30) Peelaers, H.; Van De Walle, C. G. Effects of Strain on Band Structure and Effective Masses in MoS_2. *Phys. Rev. B: Condens. Matter Mater. Phys.* **2012**, *86*, 241401.

(31) Yun, W. S.; Han, S. W.; Hong, S. C.; Kim, I. G.; Lee, J. D. Thickness and Strain Effects on Electronic Structures of Transition Metal Dichalcogenides: 2H-MX_2 Semiconductors (M = Mo, W; X = S, Se, Te). *Phys. Rev. B: Condens. Matter Mater. Phys.* **2012**, *85*, 033305.

(32) Liu, G.-B.; Shan, W. Y.; Yao, Y.; Yao, W.; Xiao, D. Three-Band Tight-Binding Model for Monolayers of Group-VIB Transition Metal Dichalcogenides. *Phys. Rev. B: Condens. Matter Mater. Phys.* **2013**, *88*, 85433.

(33) Ye, H.; Zhou, J.; Er, D.; Price, C. C.; Yu, Z.; Liu, Y.; Lowengrub, J.; Lou, J.; Liu, Z.; Shenoy, V. B. Toward a Mechanistic Understanding of Vertical Growth of van Der Waals Stacked 2D Materials: A Multiscale Model and Experiments. *ACS Nano* **2017**, *11*, 12780−12788.

(34) Hu, W.; Yang, J. Two-Dimensional van Der Waals Heterojunctions for Functional Materials and Devices. *J. Mater. Chem. C* **2017**, *5*, 12289.

(35) Yang, K.; de Llano, M. Simple Variational Proof That Any Two-dimensional Potential Well Supports at Least One Bound State. *Am. J. Phys.* **1989**, *57*, 85−86.

(36) Huang, H.; Fu, X.-Q.; Han, R.-S. Klein Paradox of Two-Dimensional Dirac Electrons in Circular Well Potential. *Commun. Theor. Phys.* **2012**, *58*, 205−208.

(37) Benguria, R. D.; Castillo, H.; Benguria, R. D.; Loewe, M. The Dirac Equation with a δ-Potential. *J. Phys. A: Math. Gen.* **2000**, *33*, 5315−5320.

DOI: 10.1021/acsnano.9b03716
ACS Nano 2019, 13, 8303−8311

(38) Divincenzo, D. P.; Mele, E. J. Self-Consistent Effective-Mass Theory for Intralayer Screening in Graphite Intercalation Compounds. *Phys. Rev. B: Condens. Matter Mater. Phys.* **1984**, *29*, 1685–1694.
(39) Schmidt, H.; Wang, S.; Chu, L.; Toh, M.; Kumar, R.; Zhao, W.; Castro Neto, A. H.; Martin, J.; Adam, S.; Özyilmaz, B.; Eda, G. Transport Properties of Monolayer MoS_2 Grown by Chemical Vapor Deposition. *Nano Lett.* **2014**, *14*, 1909–1913.
(40) Shi, Y.; Zhou, W.; Lu, A.-Y.; Fang, W.; Lee, Y.-H.; Hsu, A. L.; Kim, S. M.; Kim, K. K.; Yang, H. Y.; Li, L.-J.; Idrobo, J.-C.; Kong, J. Van Der Waals Epitaxy of MoS_2 Layers Using Graphene as Growth Templates. *Nano Lett.* **2012**, *12*, 2784–2791.
(41) Pavlović, S.; Peeters, F. M. Electronic Properties of Triangular and Hexagonal MoS2 Quantum Dots. *Phys. Rev. B: Condens. Matter Mater. Phys.* **2015**, *91*, 155410.
(42) Messias De Resende, B.; Crasto De Lima, F.; Miwa, R. H.; Vernek, E.; Ferreira, G. J. Confinement and Fermion Doubling Problem in Dirac-like Hamiltonians. *Phys. Rev. B: Condens. Matter Mater. Phys.* **2017**, *96*, 161113.
(43) Helveg, S.; Lauritsen, J. V.; Laegsgaard, E.; Stensgaard, I.; Nørskov, J. K.; Clausen, B. S.; Topsøe, H.; Besenbacher, F. Atomic-Scale Structure of Single-Layer MoS_2 Nanoclusters. *Phys. Rev. Lett.* **2000**, *84*, 951–954.
(44) Lauritsen, J. V.; Bollinger, M. V.; Laegsgaard, E.; Jacobsen, K. W.; Nørskov, J. K.; Clausen, B. S.; Topsøe, H.; Besenbacher, F. Atomic-Scale Insight into Structure and Morphology Changes of MoS_2 Nanoclusters in Hydrotreating Catalysts. *J. Catal.* **2004**, *221*, 510–522.
(45) Chen, K.; Wan, X.; Wen, J.; Xie, W.; Kang, Z.; Zeng, X.; Chen, H.; Xu, J.-B. Electronic Properties of MoS_2–WS_2 Heterostructures Synthesized with Two-Step Lateral Epitaxial Strategy. *ACS Nano* **2015**, *9*, 9868–9876.
(46) Hafeez, M.; Gan, L.; Li, H.; Ma, Y.; Zhai, T. Chemical Vapor Deposition Synthesis of Ultrathin Hexagonal $ReSe_2$ Flakes for Anisotropic Raman Property and Optoelectronic Application. *Adv. Mater.* **2016**, *28*, 8296–8301.
(47) Hong Ng, V. M.; Huang, H.; Zhou, K.; Lee, P. S.; Que, W.; Xu, J. Z.; Kong, L. B. Recent Progress in Layered Transition Metal Carbides and/or Nitrides (MXenes) and Their Composites: Synthesis and Applications. *J. Mater. Chem. A* **2017**, *5*, 3039–3068.
(48) Choi, W.; Choudhary, N.; Han, G. H.; Park, J.; Akinwande, D.; Lee, Y. H. Recent Development of Two-Dimensional Transition Metal Dichalcogenides and Their Applications. *Mater. Mater. Today* **2017**, *20*, 116–130.
(49) Zhou, W.; Zhang, Y.-Y.; Chen, J.; Li, D.; Zhou, J.; Liu, Z.; Chisholm, M. F.; Pantelides, S. T.; Loh, K. P. Dislocation-Driven Growth of Two-Dimensional Lateral Quantum-Well Superlattices. *Sci. Adv.* **2018**, *4*, No. eaap9096.
(50) Stanford, M. G.; Pudasaini, P. R.; Cross, N.; Mahady, K.; Hoffman, A. N.; Mandrus, D. G.; Duscher, G.; Chisholm, M. F.; Rack, P. D. Tungsten Diselenide Patterning and Nanoribbon Formation by Gas-Assisted Focused-Helium-Ion-Beam-Induced Etching. *Small Methods* **2017**, *1*, 1600060.
(51) Kobayashi, Y.; Yoshida, S.; Maruyama, M.; Mogi, S.; Murase, K.; Maniwa, Y.; Takeuchi, O.; Okada, S.; Shigekawa, H.; Miyata, Y. Continuous Heteroepitaxy of Two-Dimensional Heterostructures Based on Layered Chalcogenides. *ACS Nano* **2019**, DOI: 10.1021/acsnano.8b07991.
(52) Rostami, H.; Moghaddam, A. G.; Asgari, R. Effective Lattice Hamiltonian for Monolayer MoS_2: Tailoring Electronic Structure with Perpendicular Electric and Magnetic Fields. *Phys. Rev. B: Condens. Matter Mater. Phys.* **2013**, *88*, 85440.

DOI: 10.1021/acsnano.9b03716
ACS Nano 2019, 13, 8303–8311